Tailoring Hot-Carrier Distributions of Plasmonic Nanostructures through Surface Alloying

N.B. When citing this work, cite the original published paper.

(article starts on next page)

ARTICLE

Tailoring Hot-Carrier Distributions of Plasmonic Nanostructures through Surface Alloying

Jakub Fojt, Tuomas P. Rossi, Priyank V. Kumar,* and Paul Erhart*

Read Online

ACCESS | Metrics & More | Article Recommendations | Supporting Information

ABSTRACT: Alloyed metal nanoparticles are a promising platform for plasmonically enabled hot-carrier generation, which can be used to drive photochemical reactions. Although the non-plasmonic component in these systems has been investigated for its potential to enhance catalytic activity, its capacity to affect the photochemical process favorably has been underexplored by comparison. Here, we study the impact of surface alloy species and concentration on hot-carrier generation in Ag nanoparticles. By first-principles simulations, we photoexcite the localized surface plasmon, allow it to dephase, and calculate spatially and energetically resolved hot-carrier distributions. We show that the presence of non-noble species in the topmost surface layer drastically enhances hot-hole generation at the surface at the expense of hot-hole generation in the bulk, due to the additional d-type states that are introduced to the surface. The energy of the generated holes can be tuned by choice of the alloyant, with systematic trends across the d-band block. Already low surface alloy concentrations have a large impact, with a saturation of the enhancement effect typically close to 75% of a monolayer. Hot-electron generation at the surface is hindered slightly by alloying, but here a judicious choice of the alloy composition allows one to strike a balance between hot electrons and holes. Our work underscores the promise of utilizing multicomponent nanoparticles to achieve enhanced control over plasmonic catalysis and provides guidelines for how hot-carrier distributions can be tailored by designing the electronic structure of the surface through alloying.

KEYWORDS: Hot-carrier, Time-dependent density functional theory, Plasmonic catalysis, Nanoparticles, Alloys
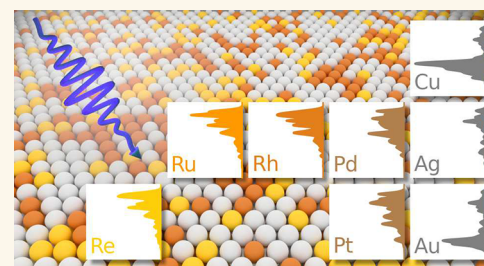
Several emerging technologies in light-harvesting,[1] solar-to-chemical energy conversion,[2−4] and catalysis[5−8] rely on hot carrier (HC) generation in plasmonic nanoparticles (NPs). During this process, light is absorbed in NPs, creating a collective electronic excitation[9] that decays into highly non-thermal electrons and holes.[2,10−23] These non-thermal carriers (usually called "hot", despite being somewhat of a misnomer[24]) prove useful when they cross some interface, for example, to a molecule or to a semiconductor, and can modify chemical reaction barriers[19] or contribute to the photocurrent in photovoltaic devices.[1] The collective electronic excitation is called a localized surface plasmon (LSP)[9] and is particularly strong in noble metal NPs, manifesting as a large optical absorption cross section at visible frequencies.[25,26] Prototypical plasmonic metals such as Ag,[8,27] Au,[3,4,28] or Cu[6,7] are used due to their outstanding optical properties. However, recently there has been increased interest in multicomponent NPs, such as antenna-reactor,[29−31] core−shell,[32] or single-atom alloys.[29,33] This interest is motivated by the fact that typical plasmonic metals (Ag, Au, or Cu) have the right optical properties but are poor traditional catalysts. In fact, using NPs

with a plasmonic core and a catalytic surface alloy, several groups[29,30,32] have achieved better photocatalytic rates than with single-component systems. Several mechanisms can lead to improved reaction rates, and as the processes take place on a picosecond or femtosecond scale, they can be hard to distinguish. Assuming that the reaction barrier is lowered by an occupation change in an orbital of the reactant,[19] the charge transfer can take place either directly by the LSP dephasing into a charge transfer excitation[24,27,34,35] or indirectly by scattering of a HC from the reactive surface of the NP. In the latter case, HCs need to be generated at the surface (directly through the decay of the LSP or through electromagnetic field enhancement, often called plasmon induced resonant energy
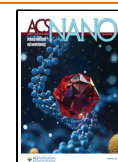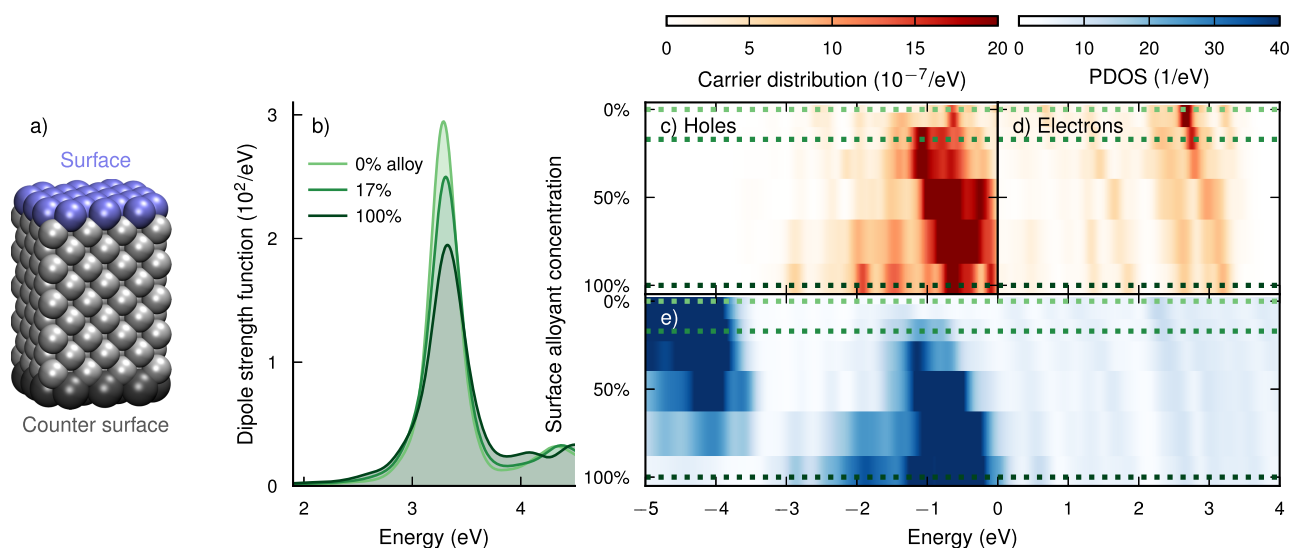
Figure 1. Distribution of hot carriers at the surface of Ag−Pt NPs as a function of composition. (a) NP geometry studied here, with the top surface marked, which is alloyed and where the carrier distributions are evaluated. **(b)** Absorption spectra of Ag−Pt NPs with different Pt surface concentrations. **(c)** Hole and **(d)** electron distributions at the top surface after resonant laser excitation as a function of surface composition. **(e)** Projected DOS (PDOS) of the top surface. The dotted lines in (c−e) correspond to the spectra shown in (b).
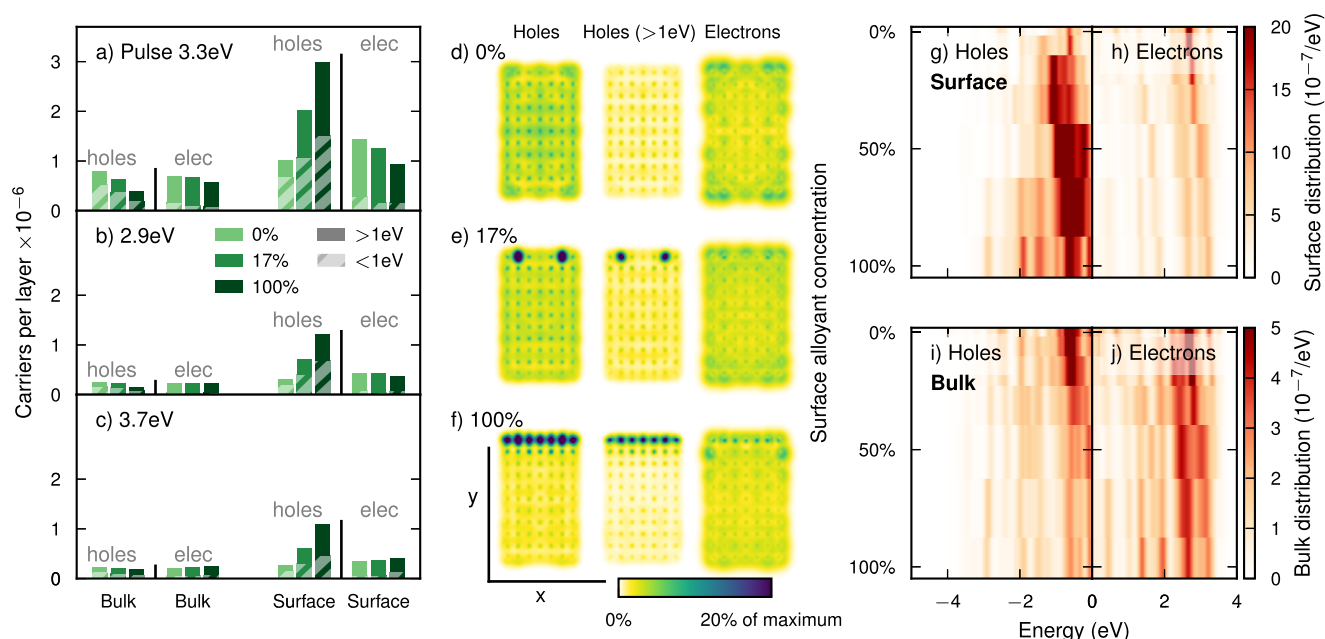

Figure 2. Hot carrier distribution in Ag−Pt NPs as a function of pulse energy and location. (a−c) Number of induced carriers in the surface and bulk, respectively after resonant (3.3 eV) and off-resonant (2.9/3.7 eV) laser excitation, for the unalloyed, optimally alloyed (17%), and fully alloyed NPs. The portion of carriers with an energy of more than 1 eV relative to the Fermi level is shown by solid bars (referred to as "hot carriers" in the text). The fraction of carriers with an energy below this threshold is indicated by hatched bars. **(d−f)** Visualization of hole, hot hole, and electron densities after resonant laser excitation for unalloyed, optimally alloyed (17%), and fully alloyed NPs. The densities have been integrated over the z-direction. **(g)** Hole and **(h)** electron distributions in the surface and **(i, j)** in the bulk, as a function of surface alloy concentration.

transfer[30,36,37]) or scattered from HCs generated throughout the NP.[38] To add further complexity, all processes eventually lead to local heating, which by itself usually increases catalytic activity, and care needs to be taken to disentangle these effects experimentally.[19,39−42] Theoretical and computational modeling can provide insights into these processes, allowing the rational design of efficient devices.[12,17,20,24,35,39,43−51] Strategies for optimizing HC generation rates and tailoring HC distributions are particularly valuable.

In this work, we study the influence of surface alloying on HC generation in plasmonic Ag NPs. We find that already a modest surface alloy concentration in core−shell or core−crown configurations can enhance the generation of hot holes and that the d-band position of the alloy dictates the energy distribution of the holes. We emphasize that, in our NPs, the shell is photocatalytically active, in contrast to earlier work that considered a photoactive core and a catalytic shell.[32,52] We model plasmon decay and HC formation using methods

developed in our group[18,20−22] based on real-time time-dependent density functional theory (RT-TDDFT).[53] We drive our systems with an ultrashort laser pulse, simulate the electron dynamics until the plasmon has decayed, and then analyze the distribution of carriers over the ground state Kohn−Sham (KS) states. The dephasing process of the LSP into HCs has been studied in detail before in refs 20 and 35, which also provide a detailed description of the methodology.

RESULTS AND DISCUSSION

Tuning the HC Distribution via Surface Composition: Getting the Holes to the Surface. We study the influence of alloying on HC formation by considering a few geometrically identical NPs. We compare unalloyed Ag with core−crown Ag−Pt NPs where substitutions are made in the top surface (Figure 1a). The NPs consist of 7-by-11 atomic layers (1.2 nm-by-2 nm) of a fcc lattice, with 24 atoms in the surface layer and 245 atoms in the bulk. The lattice parameter is 4.09 Å and we have not relaxed the structures, in order to study the effect of chemistry and not local geometry effects. These NPs have a LSP resonance at 3.3 eV corresponding to excitation along their long axis (Figure 1b). The maximum of the LSP decreases while the peak broadens with increasing surface alloy concentration, in agreement with experiment.[32]

The surface hole distribution (Figure 1c, where the "surface" is defined in Figure 1a), following resonant LSP excitation (laser pulse $\hbar\omega_{pulse}$ = 3.3 eV), depends sensitively on the alloy concentration: The unalloyed NP has relatively few holes in the surface, in the energy range between $-\hbar\omega_{pulse}$ and 0 eV. Already a modest surface alloy concentration of 17% (4 atoms swapped; Figure S1) greatly increases the hole distribution, in particular between −1.5 and −0.5 eV. While the total number of holes (i.e., the integral of the distribution) *increases* with surface alloy concentration, the peak of the distribution also shifts closer to the Fermi level, thus yielding "colder" holes. In contrast, the total number of surface electrons *decreases* as Pt is added to the surface (Figure 1d), while the distribution shifts to higher energies, corresponding to "hotter" electrons.

The projected DOS (PDOS) in the surface layer (Figure 1e) indicates which surface states are available. In the unalloyed NP, the PDOS consists of many occupied and unoccupied Ag sp-states above about −4 eV as well as d-states below approximately −4 eV. The latter states do not appear in the hole distribution, as they are further away from the Fermi level than the energy supplied by the resonant laser pulse (3.3 eV). As Pt is substituted into the surface, Pt d-states appear between −1.5 and −0.5 eV, while the number of Ag d-states (around −4 eV) decreases. The gradual shift of a Ag-like d-band to a Pt-like d-band with increasing concentration coincides with the increased amount of hole formation after resonant laser excitation. With increasing Pt concentration, additionally the sp-states shift to higher energies, which is reflected in the electrons becoming "hotter". We note that, while for the 269-atom NP studied here, which is about 2 nm in size, the density of states is discrete, for larger NPs, it would approach a continuum.

Why Does It Work: Localizing the Holes at the Surface. For alloyed NPs, the increase in *hole carriers* at the surface comes at the expense of holes in the bulk (Figure 2a; see also Figure 3). While the number of holes at the surface doubles (100% increase) for a 17% surface alloy coverage compared to the unalloyed NP, the number of holes in the bulk is reduced by 20%. This also applies to "hot" holes, which
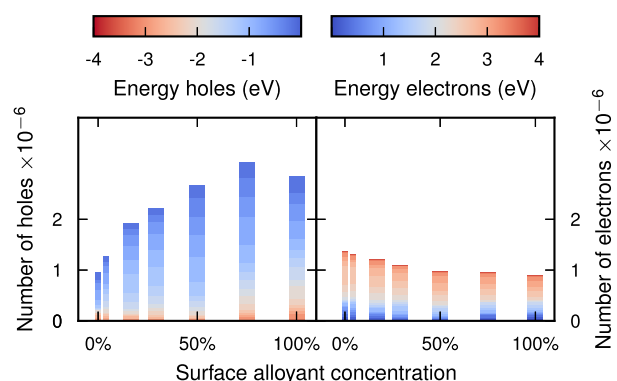

Figure 3. Number of HCs at the surface of the core−crown Ag−Pt NP for different surface alloy compositionsby energetic range after excitation with a laser at the LSP peak (3.3 eV).

we here define as hole states with an energy of more than 1 eV below the Fermi energy. The concentration of the latter is enhanced almost 3-fold (183%) at the surface, while their concentration in the bulk is reduced by 2% compared to the pure Ag NP. In the fully alloyed surface, these numbers increase to 196%/337% for all/hot holes in the surface and a reduction of 50%/24% in the bulk. Alloying thus pulls holes from the bulk to the alloyed surface, while the total number of holes decreases somewhat due to the broader LSP resonance (Figure 1b).

The total number of *excited electrons* is also decreased by alloying, but the decrease is more severe in the surface than in the bulk (Figure 2a). Hence there is a trade-off when alloying between increasing the amount of holes or electrons in the surface, such that at, e.g., 17% surface alloy concentration one can excite both many electrons and holes (Figure 3). Similar trends are observed for the hole distribution when exciting the system using an off-resonant pulse (Figure 2b,c), while the electron distributions change less systematically.

Electrons and holes differ qualitatively in how they are affected by alloying because electrons always populate sp-states, which are delocalized in character, and holes may populate the Pt d-type states, which are localized. In the unalloyed NP, holes, hot holes, and electrons are fairly evenly distributed over the NP (Figure 2d). The electrons are only in slight excess at the edges of the NP, which is due to preferential localization of carriers to undercoordinated surface sites.[20] In the NPs with surface alloy concentrations of 17% and 100%, a large fraction of holes and hot holes are localized at alloy sites, while the density of electrons remains relatively uniform (Figure 2e,f). The localization of holes at the surface also becomes apparent by comparing the surface hole distribution (Figure 2g) to the bulk hole distribution (Figure 2i), where the former even shows a non-monotonic variation with composition. In contrast, electron distributions in the surface (Figure 2h) and bulk (Figure 2j) are similar to each other because they are delocalized over the entire NP. The electron distributions are relatively unaffected by alloying except for an overall shift of states and decrease in intensity.

The number of hole carriers at the surface increases with alloying until it reaches a maximum at 75% alloy concentration (Figure 3), with the steepest increase at low concentrations. To understand why the increase is not simply linear with the alloy concentration (even after compensating for the lowered absorption; see Figure S2), as one might expect, the mechanism of carrier formation has to be considered. Carriers

are formed in pairs after plasmon decay, with the energetic difference between electron and hole equal to $\hbar\omega_{pulse}$.[35] (Note that we do not consider electron–electron or electron–phonon scattering processes in our calculations.) The pulse frequency and width thus determine which electron hole pairs can form. However, the probability of electron–hole pair formation depends additionally on the coupling strength of the pair to the LSP. The saturation of hole formation at high concentrations could thus be caused by screening of the d-type holes and their interaction with the LSP.

For completeness, we also consider alloying of more than one full surface layer on one side of the NP (core–crown alloy) as well as layers on both sides (core–shell alloying; Figure S3 and Figure S4). As expected, this increases the total amount of holes in the surface (counting all alloyed layers), but there are fewer holes per layer due to the further decreased absorption.

We note that we can also generate holes in the d-band of Ag by using pulses that are sufficiently energetic to excite transitions to unoccupied states, i.e., for $\gtrsim 3.8$ eV. The resulting hole densities are, however, notably lower than those for less energetic pulses, and the holes form predominantly in the bulk (Figure S5). Highly energetic holes in the bulk are usually not the intended outcome, so this is not so relevant for the Ag-core–Pt-shell system. It could, however, be of interest in, e.g., core–shell structures with an Ag shell and a core lacking a d-band (e.g., Al).

Finally, we emphasize here that the numbers presented in this section are specific to the NP shape considered, yet the trends in HC distributions with alloyant concentration are universal. To demonstrate this behavior one can repeat the above analysis for NPs extended along and/or perpendicular to the long axis. While the maxima of the absorption spectra naturally change with aspect ratio (and size), the broadening and blueshift with increased alloying is consistent among all four NPs considered here (Figure S6). Importantly the spectrum of the 50% surface alloy is already very close to the spectrum of the 100% surface alloy, a trend that can also be observed in bulk alloys between groups 10 (Pd, Pt) and 11 (Cu, Ag, Au).[54]

When it comes to the distribution of the number of carriers in the surface layer, one finds that, for all four sizes considered here, the number of holes increases greatly while the number of electrons decreases slightly with increasing surface alloyant concentration (Figure S7 and Figure S8). Moreover, the increase in the number of holes is greatest between 0 and 50%, echoing the composition dependence observed for the spectra. As discussed in more detail in refs 54 and 55, one can understand this trend with composition as being the result of the gradual filling/depletion of the d-band when starting from the pure group-10/group-11 element. This analysis thus demonstrates that the trends observed here are not strongly affected by NP size or shape and largely represent the behavior of the surface (as opposed to the full NP).

Tuning the HC Distribution through Chemistry: Moving the Distribution in Energy. It is now instructive to explore the effect of the character of the alloyant on the hot carrier distribution. We expect to observe the same trends for all surface alloyant concentrations, and therefore focus on 17%, which has a good balance between increased surface electron and hole generation. To this end, we compare the HC distribution for seven different alloyants from the d-block of the periodic table while keeping the pulse frequency fixed to

the LSP peak (Figure 4a,b and Figure 5). The PDOS in the surface layer (Figure 4c) shows the d-states of the alloyant
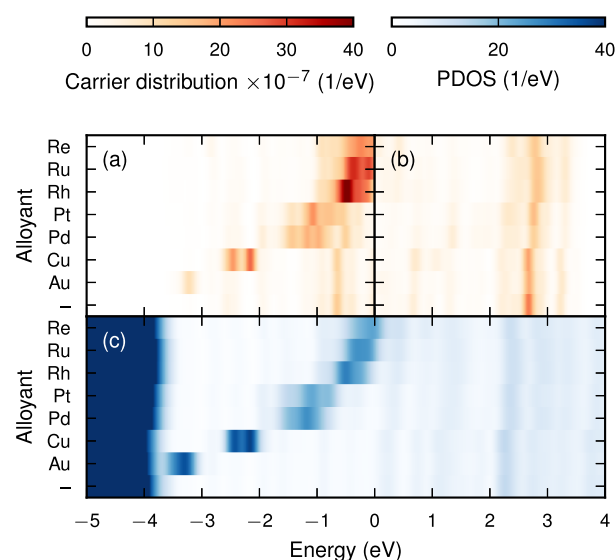

Figure 4. Variation of hot carrier distribution with alloyant. (a) Hole and (b) electron distributions for Ag-alloy NPs with a surface composition of 17% after excitation with a laser at the LSP peak (3.3 eV). (c) PDOS in the top surface layer.
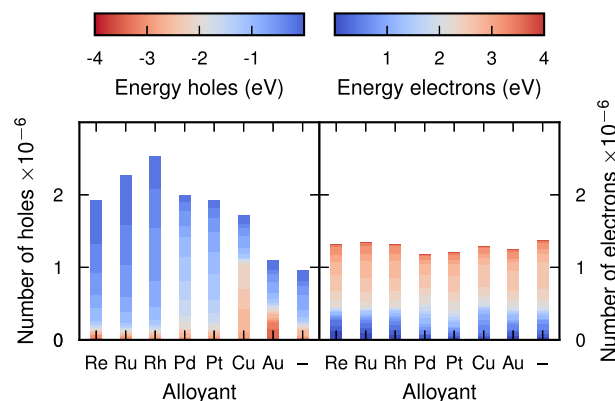

Figure 5. Number of hot carriers in the top surface for Ag-alloy NPs with a surface composition of 17% after excitation with a laser at the LSP peak (3.3 eV).

shifting closer to the Fermi level as the alloyant is found further to the left in the periodic table, i.e., as the number of electrons in the outermost d-shell of the alloyant decreases.

The hole distribution appears to be a mixture of the bare Ag NP hole distribution (holes between −1 and −0.5 eV, corresponding to sp-states) and holes in the d-states of the alloyant, which is to be expected, as the surface consists of both Ag and alloyant atoms.

The energetic distribution of electrons is almost independent of the alloyant, as the valence band structure is relatively similar for all considered alloys and because the unoccupied states are delocalized over the entire NP. The variation of the hot carrier distribution with surface concentration is similar as in the case of Pt (Figure S9).

The working principle of HC generation in these NPs is that a LSP is induced in the Ag core by absorbing light and decays into excited electron–hole pairs. The electron–hole pairs consist of both intraband sp–sp transitions and interband d–

sp transitions, where the former are entirely delocalized and the latter consist of localized holes and delocalized electrons. The alloyants provide occupied d-states at the surface, allowing holes to form. By controlling the alloyant concentration and species the hot-hole distribution can thus be tuned (Figure 6).
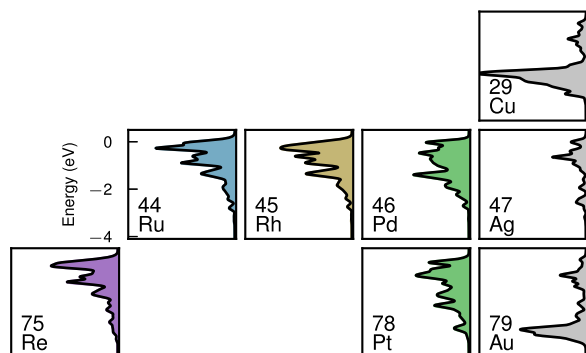

Figure 6. Hot hole distribution at the surface of Ag-alloy NPs with a surface composition of 17% after excitation with a laser at the LSP peak (3.3 eV).

The group 10 transition metals Pt and Pd produce holes between −2 and 0 eV. Moving to the left of the d-block of the periodic table, the d-band shifts closer to the Fermi level, so that the group 9, 8, and 7 elements Rh, Ru, and Re generate holes between −1 and 0 eV.

CONCLUSIONS AND OUTLOOK

We have modeled core−crown NPs with plasmonic Ag cores and transition metal crowns. Our results show that core−crown alloying can be effective for enhancing HC distributions at the surface of nanostructures. In particular, we have shown that the type of alloyant influences the energy of the holes in the resulting surface hot-hole distribution (Figure 6) but has a very minor impact on the surface hot-electron distribution. The alloyant surface concentration determines the intensity of the HC distributions, as the number of induced holes increases with concentration while the number of electrons decreases.

In general, alloying broadens the optical absorption peak, and thus typically reduces the amount of energy absorbed when exciting the system with a laser resonant with the LSP. In part because of the lower absorption, the amount of excited electrons decreases with alloyant concentration. One should, however, probably also consider the additional effect of the intraband transitions coupling more weakly to the LSP when alloying. The mechanism of such an effect is hard to pinpoint. Despite the lower total absorption, the amount of holes increases non-linearly with increasing surface alloy concentration and saturates around 75%. The saturation could be explained by the presence of many holes in d-states screening the coupling between the plasmon and the interband transitions.

Based on our results, we would suggest to design as thin shells as possible in core−shell setups. Alloying less than one full layer is actually preferable as this approach enables the biggest gains in hot-hole enhancement without suffering a big loss in hot-electron generation. Even if for larger NPs the optical spectrum is not as significantly affected, there is the presumed effect of screening of the interband transitions.

In our work, the HC distributions reach a steady state after a few tens of femtoseconds, because our model does not include decay channels such as re-emission, Auger scattering (would require a non-adiabatic exchange correlation (XC)-kernel), or electron−phonon scattering. For the HCs to do any useful work, such as catalyzing a chemical reaction, they would need to transfer across the interface to another system, possibly undergoing scattering processes in the NP, a process that may take several picoseconds.[56] From an application point of view, the observable of interest would be the rate of HC transfer to the system of interest (or the catalytic rate) that is in competition with the various decay channels. Modeling these processes is beyond the scope of our work. Despite studies showing that relaxation times are somewhat dependent on alloyant,[23,57] we can expect that a higher steady state HC distribution (that is barring the decay channels) predicted in our work corresponds to a higher catalytic rate.

The HC distributions depend weakly on the pulse frequency, in the sense that the intensity, but not the shape, changes. We thus expect our analysis using a narrow Gaussian laser pulse in resonance with the LSP to also be applicable for absorption of solar light.

METHODS

Computational Details. The open-source GPAW[58,59] code package was used for all calculations. KS density functional theory ground state calculations were performed within the projector augmented wave[60] formalism using linear combination of atomic orbitals (LCAO) basis sets;[61] the *pvalence*[62] basis set, which is optimized to represent bound unoccupied states, was used for the metal species. The PBE[63,64] functional with a Hubbard $+U$ correction[65] in the form by Dudarev et al.[66] was used, with U values of 3.5 eV for Ag, 2.5 eV for Au, and 4.5 eV for Cu. A simulation cell of 25.6 Å × 25.6 Å × 38.4 Å was used to represent wave functions, XC, and Coulomb potentials, with a grid spacing of 0.2 Å for wave functions and 0.1 Å for potentials. The Coulomb potential was represented in numerical form on the grid, with an additional analytic moment correction[67] centered at the NP. Fermi−Dirac occupation number smearing with width 0.05 eV was used. The self-consistent loop was stopped when the integral of the difference between two subsequent densities was less than 1×10^{-12}. Pulay[68]-mixing was used to accelerate the ground state convergence.

The LCAO-RT-TDDFT implementation[62] in GPAW was used for the RT-TDDFT calculations. A δ-kick strength of $K_z = 10^{-5}$ in atomic units was used. The time propagation was done in steps of 10 as for a total length of 30 fs using the adiabatic PBE+U kernel. We computed the carrier generation for an external electric field corresponding to an ultrashort Gaussian laser pulse

$$\mathcal{E}_z(t) = \mathcal{E}_0 \cos(\omega_0 t) \exp(-(t - t_0)^2 / 2\,\tau_0{}^2) \qquad (1)$$

of frequency ω, strength $\mathcal{E}_0 = 0.1$ mV Å^{-1}, peak time $t_0 = 10$ fs, and duration $\tau_0 = 2.1$ fs. Following the methods of refs 20 and 35, the computation of hot carrier generation was carried out by convoluting the first order density response of the δ-kick-calculation with the laser pulse, and the hot-carrier distributions were projected according to the atomic layer Voronoi weights.

We computed the total density of states as

$$\sum_k \delta(\varepsilon - \varepsilon_k) \qquad (2)$$

and the PDOS for the atomic layers as

$$\sum_k \delta(\varepsilon - \varepsilon_k) \int_{\text{layer}} |\phi_k^{(0)}(\mathbf{r})|^2 \, d\mathbf{r} \qquad (3)$$

where ε_k and $\phi_k^{(0)}(\mathbf{r})$ are the KS eigenvalues and wave functions. For visualization, the δ-functions in energy were replaced by a Gaussian $(2\pi\sigma^2)^{-1/2} \exp(-\varepsilon^2/2\sigma^2)$ with width $\sigma = 0.07$ eV.

SOFTWARE USED

The GPAW package[58,59] with LCAO basis sets[61] and the LCAO-RT-TDDFT implementation[62] was used for the RT-TDDFT calculations. The PBE[63,64] XC-functional, utilizing the Libxc[69] library, was used in GPAW. The ASE library[70] was used for constructing and manipulating atomic structures. The NumPy,[71] SciPy,[72] and Matplotlib[73] Python packages and the VMD software[74,75] were used for processing and plotting data.

ASSOCIATED CONTENT

Data Availability Statement

The data generated in this study are openly available via Zenodo at https://doi.org/10.5281/zenodo.10047664.

ⓢ Supporting Information

The Supporting Information is available free of charge at https://pubs.acs.org/doi/10.1021/acsnano.3c11418.

> Geometry of surface alloys; plots of the number of generated surface carriers normalized by absorbed energy; plots of spatially resolved carrier distributions throughout the NPs, for few-layer alloys; plots of spectra and HC distributions of different shapes of alloyed NPs; and bar plots of HC distributions in different alloyants and different alloyant concentrations (PDF)

AUTHOR INFORMATION

Corresponding Authors

Priyank V. Kumar − *School of Chemical Engineering, The University of New South Wales, 2052 Sydney, NSW, Australia;* ⓞ orcid.org/0000-0002-8203-7223; Email: priyank.kumar@unsw.edu.au

Paul Erhart − *Department of Physics, Chalmers University of Technology, SE-412 96 Gothenburg, Sweden;* ⓞ orcid.org/0000-0002-2516-6061; Email: erhart@chalmers.se

Authors

Jakub Fojt − *Department of Physics, Chalmers University of Technology, SE-412 96 Gothenburg, Sweden;* ⓞ orcid.org/0000-0002-8372-3153

Tuomas P. Rossi − *Department of Applied Physics, Aalto University, FI-00076 Aalto, Finland;* ⓞ orcid.org/0000-0002-8713-4559

Complete contact information is available at:
https://pubs.acs.org/10.1021/acsnano.3c11418

Notes

The preprint version of this article is the following: Fojt, J.; Rossi, T. P.; Kumar, P. V.; Erhart, P. Tailoring hot-carrier distributions of plasmonic nanostructures through surface alloying. 2023, arXiv 2311.09996. 10.48550/arXiv.2311.09996 (accessed February 8, 2024).

The authors declare no competing financial interest.

ACKNOWLEDGMENTS

REFERENCES

(1) Geng, X.; Abdellah, M.; Bericat Vadell, R.; Folkenant, M.; Edvinsson, T.; Sá, J. Direct Plasmonic Solar Cell Efficiency Dependence on Spiro-OMeTAD Li-TFSI Content. *Nanomaterials* **2021**, *11*, 3329.

(2) Aslam, U.; Rao, V. G.; Chavez, S.; Linic, S. Catalytic Conversion of Solar to Chemical Energy on Plasmonic Metal Nanostructures. *Nat. Catal.* **2018**, *1*, 656−665.

(3) Li, R.; Cheng, W.-H.; Richter, M. H.; DuChene, J. S.; Tian, W.; Li, C.; Atwater, H. A. Unassisted Highly Selective Gas-Phase CO2 Reduction with a Plasmonic Au/p-GaN Photocatalyst Using H2O as an Electron Donor. *ACS Energy Lett.* **2021**, *6*, 1849−1856.

(4) DuChene, J. S.; Tagliabue, G.; Welch, A. J.; Cheng, W.-H.; Atwater, H. A. Hot Hole Collection and Photoelectrochemical CO2 Reduction with Plasmonic Au/p-GaN Photocathodes. *Nano Lett.* **2018**, *18*, 2545−2550.

(5) Zhou, L.; Lou, M.; Bao, J. L.; Zhang, C.; Liu, J. G.; Martirez, J. M. P.; Tian, S.; Yuan, L.; Swearer, D. F.; Robatjazi, H.; Carter, E. A.; Nordlander, P.; Halas, N. J. Hot Carrier Multiplication in Plasmonic Photocatalysis. *Proc. Natl. Acad. Sci. U.S.A.* **2021**, *118*, No. e2022109118.

(6) DuChene, J. S.; Tagliabue, G.; Welch, A. J.; Li, X.; Cheng, W.-H.; Atwater, H. A. Optical Excitation of a Nanoparticle Cu/p-NiO Photocathode Improves Reaction Selectivity for CO2 Reduction in Aqueous Electrolytes. *Nano Lett.* **2020**, *20*, 2348−2358.

(7) Hou, T.; Chen, L.; Xin, Y.; Zhu, W.; Zhang, C.; Zhang, W.; Liang, S.; Wang, L. Porous CuFe for Plasmon-Assisted N2 Photofixation. *ACS Energy Lett.* **2020**, *5*, 2444−2451.

(8) Yamazaki, Y.; Kuwahara, Y.; Mori, K.; Kamegawa, T.; Yamashita, H. Enhanced Catalysis of Plasmonic Silver Nanoparticles by a Combination of Macro-/Mesoporous Nanostructured Silica Support. *J. Phys. Chem. C* **2021**, *125*, 9150−9157.

(9) Kreibig, U.; Vollmer, M. *Optical Properties of Metal Clusters*; Springer Series in Materials Science *25*; Springer: Berlin, 1995.

(10) Brongersma, M. L.; Halas, N. J.; Nordlander, P. Plasmon-Induced Hot Carrier Science and Technology. *Nat. Nanotechnol.* **2015**, *10*, 25−34.

(11) Gong, T.; Munday, J. N. Materials for Hot Carrier Plasmonics [Invited]. *Optical Materials Express* **2015**, *5*, 2501−2512.

(12) Román Castellanos, L.; Hess, O.; Lischner, J. Single Plasmon Hot Carrier Generation in Metallic Nanoparticles. *Commun. Phys.* **2019**, *2*, 1−9.

(13) Khurgin, J. B. Hot Carriers Generated by Plasmons: Where Are They Generated and Where Do They Go from There? *Faraday Discuss.* **2019**, *214*, 35−58.

(14) Khurgin, J. B. Fundamental Limits of Hot Carrier Injection from Metal in Nanoplasmonics. *Proc. Spie* **2020**, *9*, 453−471.

(15) Hattori, Y.; Meng, J.; Zheng, K.; Meier de Andrade, A.; Kullgren, J.; Broqvist, P.; Nordlander, P.; Sá, J. Phonon-Assisted Hot Carrier Generation in Plasmonic Semiconductor Systems. *Nano Lett.* **2021**, *21*, 1083−1089.

(16) Hawe, P.; Silveira, V. R. R.; Bericat Vadell, R.; Lewin, E.; Sá, J. Plasmon-Mediated Oxidation Reaction on Au/p-Cu2O: The Origin of Hot Holes. *Physchem* **2021**, *1*, 163−175.

(17) Bernardi, M.; Mustafa, J.; Neaton, J. B.; Louie, S. G. Theory and Computation of Hot Carriers Generated by Surface Plasmon Polaritons in Noble Metals. *Nat. Commun.* **2015**, *6*, 7044.

(18) Rossi, T. P.; Kuisma, M.; Puska, M. J.; Nieminen, R. M.; Erhart, P. Kohn−Sham Decomposition in Real-Time Time-Dependent Density-Functional Theory: An Efficient Tool for Analyzing Plasmonic Excitations. *J. Chem. Theory Comput.* **2017**, *13*, 4779−4790.

(19) Zhou, L.; Swearer, D. F.; Zhang, C.; Robatjazi, H.; Zhao, H.; Henderson, L.; Dong, L.; Christopher, P.; Carter, E. A.; Nordlander, P.; Halas, N. J. Quantifying Hot Carrier and Thermal Contributions in Plasmonic Photocatalysis. *Science* **2018**, *362*, 69−72.

(20) Rossi, T. P.; Erhart, P.; Kuisma, M. Hot-Carrier Generation in Plasmonic Nanoparticles: The Importance of Atomic Structure. *ACS Nano* **2020**, *14*, 9963−9971.

(21) Kumar, P. V.; Rossi, T. P.; Kuisma, M.; Erhart, P.; Norris, D. J. Direct Hot-Carrier Transfer in Plasmonic Catalysis. *Faraday Discuss.* **2019**, *214*, 189−197.

(22) Kumar, P. V.; Rossi, T. P.; Marti-Dafcik, D.; Reichmuth, D.; Kuisma, M.; Erhart, P.; Puska, M. J.; Norris, D. J. Plasmon-Induced Direct Hot-Carrier Transfer at Metal−Acceptor Interfaces. *ACS Nano* **2019**, *13*, 3188−3195.

(23) Villegas, C. E. P.; Leite, M. S.; Marini, A.; Rocha, A. R. Efficient Hot-Carrier Dynamics in near-Infrared Photocatalytic Metals. *Phys. Rev. B* **2022**, *105*, 165109.

(24) Khurgin, J. B.; Petrov, A.; Eich, M.; Uskov, A. V. Direct Plasmonic Excitation of the Hybridized Surface States in Metal Nanoparticles. *ACS Photonics* **2021**, *8*, 2041−2049.

(25) Bohren, C. F. How Can a Particle Absorb More than the Light Incident on It? *Am. J. Phys.* **1983**, *51*, 323−327.

(26) Langhammer, C.; Kasemo, B.; Zorić, I. Absorption and Scattering of Light by Pt, Pd, Ag, and Au Nanodisks: Absolute Cross Sections and Branching Ratios. *J. Chem. Phys.* **2007**, *126*, 194702.

(27) Christopher, P.; Xin, H.; Linic, S. Visible-Light-Enhanced Catalytic Oxidation Reactions on Plasmonic Silver Nanostructures. *Nat. Chem.* **2011**, *3*, 467−472.

(28) Saha, S.; Yang, J.; Masouleh, S. S. M.; Botton, G. A.; Soleymani, L. Hot Hole Direct Photoelectrochemistry of Au NPs: Interband versus Intraband Hot Carriers. *Electrochim. Acta* **2022**, *404*, 139746.

(29) Zhou, L.; Martirez, J. M. P.; Finzel, J.; Zhang, C.; Swearer, D. F.; Tian, S.; Robatjazi, H.; Lou, M.; Dong, L.; Henderson, L.; Christopher, P.; Carter, E. A.; Nordlander, P.; Halas, N. J. Light-Driven Methane Dry Reforming with Single Atomic Site Antenna-Reactor Plasmonic Photocatalysts. *Nature Energy* **2020**, *5*, 61−70.

(30) Ren, H.; Yang, J.-L.; Yang, W.-M.; Zhong, H.-L.; Lin, J.-S.; Radjenovic, P. M.; Sun, L.; Zhang, H.; Xu, J.; Tian, Z.-Q.; Li, J.-F. Core−Shell−Satellite Plasmonic Photocatalyst for Broad-Spectrum Photocatalytic Water Splitting. *ACS Materials Letters* **2021**, *3*, 69−76.

(31) Jin, H.; Herran, M.; Cortés, E.; Lischner, J. Theory of Hot-Carrier Generation in Bimetallic Plasmonic Catalysts. *ACS Photonics* **2023**, *10*, 3629−3636.

(32) Aslam, U.; Chavez, S.; Linic, S. Controlling Energy Flow in Multimetallic Nanostructures for Plasmonic Catalysis. *Nat. Nanotechnol.* **2017**, *12*, 1000−1005.

(33) Sorvisto, D.; Rinke, P.; Rossi, T. P. Single-Atom Dopants in Plasmonic Nanocatalysts. *J. Phys. Chem. C* **2023**, *127*, 8585−8590.

(34) Ma, J.; Gao, S. Plasmon-Induced Electron−Hole Separation at the Ag/TiO$_2$ (110) Interface. *ACS Nano* **2019**, *13*, 13658−13667.

(35) Fojt, J.; Rossi, T. P.; Kuisma, M.; Erhart, P. Hot-Carrier Transfer across a Nanoparticle−Molecule Junction: The Importance of Orbital Hybridization and Level Alignment. *Nano Lett.* **2022**, *22*, 8786−8792.

(36) Cushing, S. K.; Li, J.; Meng, F.; Senty, T. R.; Suri, S.; Zhi, M.; Li, M.; Bristow, A. D.; Wu, N. Photocatalytic Activity Enhanced by Plasmonic Resonant Energy Transfer from Metal to Semiconductor. *J. Am. Chem. Soc.* **2012**, *134*, 15033−15041.

(37) Rudayni, F.; Kafle, T. R.; Waters, J.; Rijal, K.; Chan, W.-L. Ultrafast and Long-Range Energy Transfer from Plasmon to Molecular Exciton. *J. Phys. Chem. C* **2023**, *127*, 1697.

(38) Engelbrekt, C.; Crampton, K. T.; Fishman, D. A.; Law, M.; Apkarian, V. A. Efficient Plasmon-Mediated Energy Funneling to the Surface of Au@Pt Core−Shell Nanocrystals. *ACS Nano* **2020**, *14*, 5061−5074.

(39) Dubi, Y.; Un, I. W.; Sivan, Y. Thermal Effects − an Alternative Mechanism for Plasmon-Assisted Photocatalysis. *Chem. Sci.* **2020**, *11*, 5017−5027.

(40) Jain, P. K. Comment on "Thermal Effects − an Alternative Mechanism for Plasmon-Assisted Photocatalysis" by Y. Dubi, I. W. Un and Y. SivanSivan, Chem. Sci. , 2020, 11 , 5017. *Chem. Sci.* **2020**, *11*, 9022−9023.

(41) Sivan, Y.; Baraban, J.; Un, I. W.; Dubi, Y. Comment on "Quantifying Hot Carrier and Thermal Contributions in Plasmonic Photocatalysis". *Science* **2019**, *364*, No. eaaw9367.

(42) Zhou, L.; Swearer, D. F.; Robatjazi, H.; Alabastri, A.; Christopher, P.; Carter, E. A.; Nordlander, P.; Halas, N. J. Response to Comment on "Quantifying Hot Carrier and Thermal Contributions in Plasmonic Photocatalysis". *Science* **2019**, *364*, No. eaaw9545.

(43) Manjavacas, A.; Liu, J. G.; Kulkarni, V.; Nordlander, P. Plasmon-Induced Hot Carriers in Metallic Nanoparticles. *ACS Nano* **2014**, *8*, 7630−7638.

(44) Long, R.; Prezhdo, O. V. Instantaneous Generation of Charge-Separated State on TiO2 Surface Sensitized with Plasmonic Nanoparticles. *J. Am. Chem. Soc.* **2014**, *136*, 4343−4354.

(45) Brown, A. M.; Sundararaman, R.; Narang, P.; Goddard, W. A.; Atwater, H. A. Nonradiative Plasmon Decay and Hot Carrier Dynamics: Effects of Phonons, Surfaces, and Geometry. *ACS Nano* **2016**, *10*, 957−966.

(46) Sivan, Y.; Un, I. W.; Dubi, Y. Assistance of Metal Nanoparticles in Photocatalysis − Nothing More than a Classical Heat Source. *Faraday Discuss.* **2019**, *214*, 215−233.

(47) Román Castellanos, L.; Kahk, J. M.; Hess, O.; Lischner, J. Generation of Plasmonic Hot Carriers from D-Bands in Metallic Nanoparticles. *J. Chem. Phys.* **2020**, *152*, 104111.

(48) Chan, C. C. S.; Fan, K.; Wang, H.; Huang, Z.; Novko, D.; Yan, K.; Xu, J.; Choy, W. C. H.; Lončarić, I.; Wong, K. S. Uncovering the Electron-Phonon Interplay and Dynamical Energy-Dissipation Mechanisms of Hot Carriers in Hybrid Lead Halide Perovskites. *Adv. Energy Mater.* **2021**, *11*, 2003071.

(49) Jin, H.; Kahk, J. M.; Papaconstantopoulos, D. A.; Ferreira, A.; Lischner, J. Plasmon-Induced Hot Carriers from Interband and Intraband Transitions in Large Noble Metal Nanoparticles. *PRX Energy* **2022**, *1*, 013006.

(50) Dubi, Y.; Un, I.-W.; Sivan, Y. Distinguishing Thermal from Nonthermal ("Hot") Carriers in Illuminated Molecular Junctions. *Nano Lett.* **2022**, *22*, 2127−2133.

(51) Kluczyk-Korch, K.; Antosiewicz, T. J. Hot Carrier Generation in a Strongly Coupled Molecule−Plasmonic Nanoparticle System. *Proc. Spie.* **2023**, *12*, 1711.

(52) Robatjazi, H.; Zhao, H.; Swearer, D. F.; Hogan, N. J.; Zhou, L.; Alabastri, A.; McClain, M. J.; Nordlander, P.; Halas, N. J. Plasmon-Induced Selective Carbon Dioxide Conversion on Earth-Abundant Aluminum-Cuprous Oxide Antenna-Reactor Nanoparticles. *Nat. Commun.* **2017**, *8*, 27.

(53) Yabana, K.; Bertsch, G. F. Time-Dependent Local-Density Approximation in Real Time. *Phys. Rev. B* **1996**, *54*, 4484−4487.

(54) Rahm, J. M.; Tiburski, C.; Rossi, T. P.; Nugroho, F. A. A.; Nilsson, S.; Langhammer, C.; Erhart, P. A Library of Late Transition Metal Alloy Dielectric Functions for Nanophotonic Applications. *Adv. Funct. Mater.* **2020**, *30*, 2002122.

(55) Ekborg-Tanner, P.; Rahm, J. M.; Rosendal, V.; Bancerek, M.; Rossi, T. P.; Antosiewicz, T. J.; Erhart, P. Computational Design of Alloy Nanostructures for Optical Sensing of Hydrogen. *ACS Appl. Nano Mater.* **2022**, *5*, 10225−10236.

(56) Brown, A. M.; Sundararaman, R.; Narang, P.; Schwartzberg, A. M.; Goddard, W. A.; Atwater, H. A. Experimental and Ab Initio Ultrafast Carrier Dynamics in Plasmonic Nanoparticles. *Phys. Rev. Lett.* **2017**, *118*, 087401.

(57) Memarzadeh, S.; Palm, K. J.; Murphy, T. E.; Leite, M. S.; Munday, J. N. Control of Hot-Carrier Relaxation Time in Au-Ag Thin Films through Alloying. *Opt. Express* **2020**, *28*, 33528−33537.

(58) Mortensen, J. J.; Hansen, L. B.; Jacobsen, K. W. Real-Space Grid Implementation of the Projector Augmented Wave Method. *Phys. Rev. B* **2005**, *71*, 035109.

(59) Enkovaara, J.; Rostgaard, C.; Mortensen, J. J.; Chen, J.; Dułak, M.; Ferrighi, L.; Gavnholt, J.; Glinsvad, C.; Haikola, V.; Hansen, H.

A.; Kristoffersen, H. H.; Kuisma, M.; Larsen, A. H.; Lehtovaara, L.; Ljungberg, M.; Lopez-Acevedo, O.; Moses, P. G.; Ojanen, J.; Olsen, T.; Petzold, V.; et al. Electronic Structure Calculations with GPAW: A Real-Space Implementation of the Projector Augmented-Wave Method. *J. Phys.: Condens. Matter* **2010**, *22*, 253202.

(60) Blöchl, P. E. Projector Augmented-Wave Method. *Phys. Rev. B* **1994**, *50*, 17953−17979.

(61) Larsen, A. H.; Vanin, M.; Mortensen, J. J.; Thygesen, K. S.; Jacobsen, K. W. Localized Atomic Basis Set in the Projector Augmented Wave Method. *Phys. Rev. B* **2009**, *80*, 195112.

(62) Kuisma, M.; Sakko, A.; Rossi, T. P.; Larsen, A. H.; Enkovaara, J.; Lehtovaara, L.; Rantala, T. T. Localized Surface Plasmon Resonance in Silver Nanoparticles: Atomistic First-Principles Time-Dependent Density-Functional Theory Calculations. *Phys. Rev. B* **2015**, *91*, 115431.

(63) Perdew, J. P.; Burke, K.; Ernzerhof, M. Generalized Gradient Approximation Made Simple. *Phys. Rev. Lett.* **1996**, *77*, 3865.

(64) Perdew, J. P.; Burke, K.; Ernzerhof, M. Generalized Gradient Approximation Made Simple [Phys. Rev. Lett. 77, 3865 (1996)]. *Phys. Rev. Lett.* **1997**, *78*, 1396.

(65) Liechtenstein, A. I.; Anisimov, V. I.; Zaanen, J. Density-Functional Theory and Strong Interactions: Orbital Ordering in Mott-Hubbard Insulators. *Phys. Rev. B* **1995**, *52*, R5467−R5470.

(66) Dudarev, S. L.; Botton, G. A.; Savrasov, S. Y.; Humphreys, C. J.; Sutton, A. P. Electron-Energy-Loss Spectra and the Structural Stability of Nickel Oxide: An LSDA+U Study. *Phys. Rev. B* **1998**, *57*, 1505−1509.

(67) Castro, A.; Rubio, A.; Stott, M. J. Solution of Poisson's Equation for Finite Systems Using Plane-Wave Methods. *Can. J. Phys.* **2003**, *81*, 1151−1164.

(68) Pulay, P. Convergence Acceleration of Iterative Sequences. the Case of Scf Iteration. *Chem. Phys. Lett.* **1980**, *73*, 393−398.

(69) Lehtola, S.; Steigemann, C.; Oliveira, M. J. T.; Marques, M. A. L. Recent Developments in Libxc — A Comprehensive Library of Functionals for Density Functional Theory. *SoftwareX* **2018**, *7*, 1−5.

(70) Hjorth Larsen, A.; Jørgen Mortensen, J.; Blomqvist, J.; Castelli, I. E; Christensen, R.; Dułak, M.; Friis, J.; Groves, M. N; Hammer, B.ør.; Hargus, C.; Hermes, E. D; Jennings, P. C; Bjerre Jensen, P.; Kermode, J.; Kitchin, J. R; Leonhard Kolsbjerg, E.; Kubal, J.; Kaasbjerg, K.; Lysgaard, S.; Bergmann Maronsson, J.; et al. The Atomic Simulation Environment—a Python Library for Working with Atoms. *J. Phys.: Condens. Matter* **2017**, *29*, 273002.

(71) Harris, C. R.; Millman, K. J.; van der Walt, S. J.; Gommers, R.; Virtanen, P.; Cournapeau, D.; Wieser, E.; Taylor, J.; Berg, S.; Smith, N. J.; Kern, R.; Picus, M.; Hoyer, S.; van Kerkwijk, M. H.; Brett, M.; Haldane, A.; del Río, J. F.; Wiebe, M.; Peterson, P.; Gérard-Marchant, P.; et al. Array Programming with NumPy. *Nature* **2020**, *585*, 357−362.

(72) Virtanen, P.; Gommers, R.; Oliphant, T. E.; Haberland, M.; Reddy, T.; Cournapeau, D.; Burovski, E.; Peterson, P.; Weckesser, W.; Bright, J.; van der Walt, S. J.; Brett, M.; Wilson, J.; Millman, K. J.; Mayorov, N.; Nelson, A. R. J.; Jones, E.; Kern, R.; Larson, E.; Carey, C. J.; et al. SciPy 1.0: Fundamental Algorithms for Scientific Computing in Python. *Nat. Methods* **2020**, *17*, 261−272.

(73) Hunter, J. D. Matplotlib: A 2D Graphics Environment. *Comput. Sci. Eng.* **2007**, *9*, 90−95.

(74) Humphrey, W.; Dalke, A.; Schulten, K. VMD: Visual Molecular Dynamics. *J. Mol. Graphics* **1996**, *14*, 33−38.

(75) Stone, J. An Efficient Library for Parallel Ray Tracing and Animation. M.Sc. thesis; Computer Science Department, University of Missouri-Rolla, 1998.